Article

# Ferroelectricity with concomitant Coulomb screening in van der Waals heterostructures

Ruirui Niu[1,14], Zhuoxian Li[1,14], Xiangyan Han[1,14], Zhuangzhuang Qu[1,14], Qianling Liu[1], Zhiyu Wang[1], Chunrui Han[2]✉, Chunwen Wang[3], Yangliu Wu[4], Chendi Yang[5], Ming Lv[6], Kaining Yang[7], Kenji Watanabe[8], Takashi Taniguchi[8], Kaihui Liu[1], Jinhai Mao[9], Wu Shi[10,11], Renchao Che[5], Wu Zhou[3], Jiamin Xue[6], Menghao Wu[12], Bo Peng[4]✉, Zheng Vitto Han[7,13]✉, Zizhao Gan[1] & Jianming Lu[1]✉

Interfacial ferroelectricity emerges in non-centrosymmetric heterostructures consisting of non-polar van der Waals (vdW) layers. Ferroelectricity with concomitant Coulomb screening can switch topological currents or superconductivity and simulate synaptic response. So far, it has only been realized in bilayer graphene moiré superlattices, posing stringent requirements to constituent materials and twist angles. Here we report ferroelectricity with concomitant Coulomb screening in different vdW heterostructures free of moiré interfaces containing monolayer graphene, boron nitride (BN) and transition metal chalcogenide layers. We observe a ferroelectric hysteretic response in a BN/ monolayer graphene/BN, as well as in BN/WSe$_2$/monolayer graphene/WSe$_2$/ BN heterostructure, but also when replacing the stacking fault-containing BN with multilayer twisted MoS$_2$, a prototypical sliding ferroelectric. Our control experiments exclude alternative mechanisms, such that we conclude that ferroelectricity originates from stacking faults in the BN flakes. Hysteretic switching occurs when a conductive ferroelectric screens the gating field electrically and controls the monolayer graphene through its polarization field. Our results relax some of the material and design constraints for device applications based on sliding ferroelectricity and should enable memory device or the combination with diverse vdW materials with superconducting, topological or magnetic properties.

Artificial stacking of non-polar van der Waals (vdW) materials into interfacial ferroelectrics provides an intriguing route for constructing multi-functional vdW devices[1–7], allowing non-volatile switching of electrical/magnetic/optical properties of the non-polar constituent in a designed manner. Two branches have been developed: one is the lattice-driven sliding ferroelectricity that relies on non-centrosymmetric stacking[8–16], in which the polarization switching through interlayer sliding guarantees robust repeatability and durability; the other is the ferroelectricity with concomitant Coulomb screening observed in crystallographically aligned bilayer graphene/ boron nitride (BN) heterostructure[4,17–21], ascribed to the interlayer charge transfer induced by electronic correlation[17,19]. Especially, the latter recently was demonstrated to switch superconductivity and correlated phases[4,6]. It also works as a synaptic transistor[20] that can perform diverse biorealistic neuromorphic functionalities. The investigated materials so far have been limited to Bernal bilayer graphene[17–20], twisted bilayer graphene[4] and BN intercalated bilayer graphene[21]— why or whether is bilayer graphene unique to the ferroelectricity? In
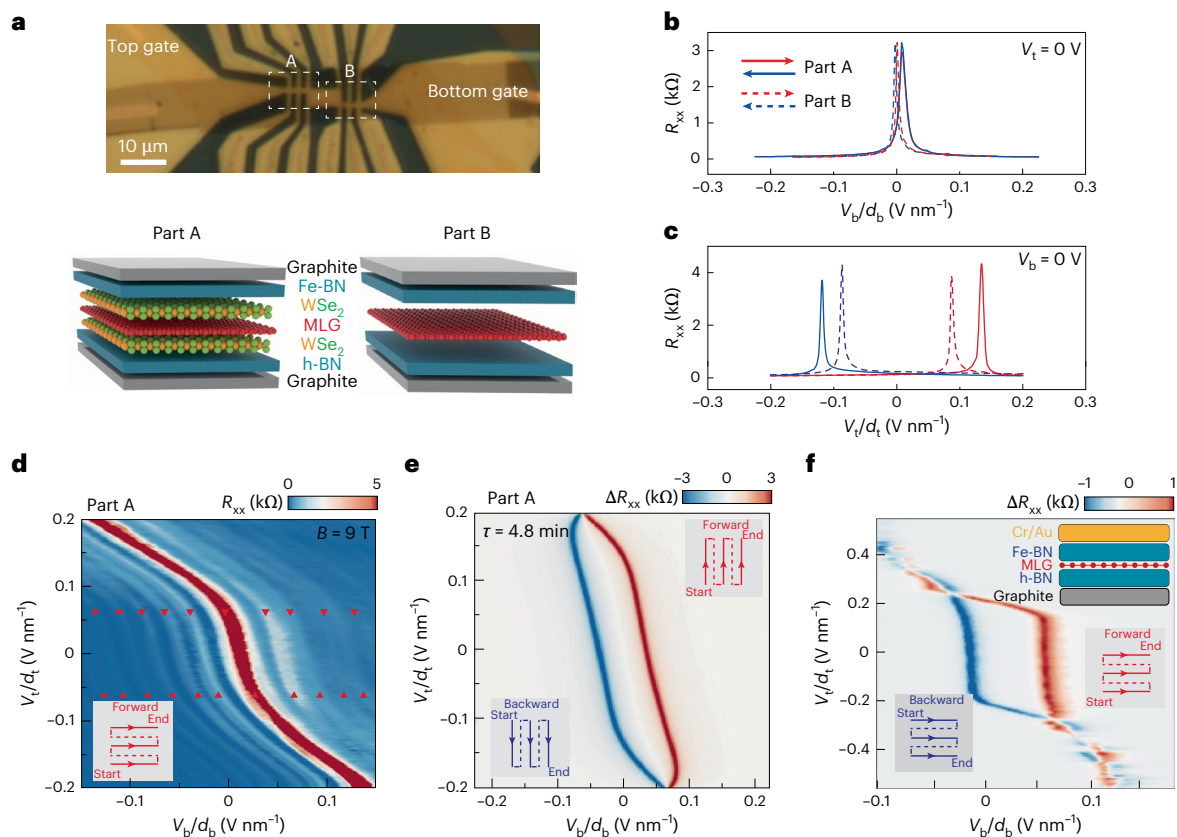
**Fig. 1 | Ferroelectricity in a monolayer graphene heterostructure. a**, Optical characterization of the device with two different parts with structure schematics. The monolayer graphene (MLG) is highlighted in red. Note that the top BN that exhibits ferroelectricity (Fe-BN) has a different notation than the bottom hexagonal BN (h-BN). **b,c**, For both Parts A and B, hysteretic resistance curves are observed by sweeping the top gate (**c**) but not by sweeping the bottom gate (**b**). **d**, Two-dimensional resistance mapping with magnetic field $B = 9$ T for Part A (see the scanning configuration in the inset). The nearly vertical feature of the CNP trajectory represents the Coulomb screening regime where $V_t$ seemingly stops working. The Landau level spectroscopy also enables visualization of electronic states with low resistances. Obviously, the Coulomb screening depends on the specific gate, that is, $V_t$ in this device (denoted by red triangles), rather than the displacement field that is contributed by both top and bottom gates. Inset: the gate scanning scheme. **e**, Hysteresis loop between forward and backward sweeping of the top gate for Part A. The relaxation time is about 4.8 min (see measurements in Supplementary Fig. 1j in Supplementary Section 1). Insets: two scanning configurations. **f**, In another device with a long relaxation time, the hysteresis loop between forward and backward sweeping of the top gate is significant. Insets: two scanning configurations and device schematic (see more characterization in Supplementary Section 2). *d*, thickness of the BN flake.

addition, ref. 18 indicates that the polarized charge density exceeds the total capacity of the moiré band, contrasting the correlation-driven mechanism where half of the moiré band can be pushed from one layer to another owing to the on-site electron–electron repulsion. The clarification of the underlying physics and the extension to other vdW materials with magnetic, superconducting and topological properties are highly desirable.

Recent findings of coexisting charge carriers and polarization in vdW ferroelectrics such as few-layer WTe₂ (refs. 8,22,23), MoTe₂ (ref. 5) and multilayer twisted MoS₂ (ref. 15) provide a novel viewpoint. (1) While the ferroelectric polarization can be switched by the gate, substantial free carriers of the ferroelectric electrically screen the bottom gate, thus isolating the top detector. (2) The polarization field of ferroelectrics, as an effective intermediate gate, solely controls the detector's electronic states. All these factors, together with microscopic characterization of electric-field-driven polarization dynamics[16,24–27], open new opportunities to tackle the long-standing puzzle.

Here we report ferroelectricity with Coulomb screening in a BN/monolayer graphene/BN, as well as in a BN/WSe₂/monolayer graphene/WSe₂/BN heterostructure, where the WSe₂ encapsulation eliminates moiré superlattices and, hence, strong correlation for electrons in graphene. Consequently, the ferroelectricity should originate instead from the particular BN flake used. Thus, we ascribe it to interfacial sliding ferroelectricity owing to the non-centrosymmetric stacking between BN layers. To substantiate the proposal, we construct a heterostructure consisting of monolayer graphene as a detector and multilayer twisted transition metal chalcogenides (MoS₂) as a part of the gate dielectric layer. The reproduced ferroelectric hysteresis in this structure-controllable device unveils the key ingredient: conductive sliding ferroelectrics. In this scenario, the electric field stemming from the gate electrode is naturally screened by the conductive ferroelectric. The graphene channel then is only subject to the electric field of polarized ferroelectrics. We demonstrate that sliding ferroelectricity is responsible for the observed ferroelectricity with Coulomb screening in monolayer graphene devices, which mitigates restrictions for device construction while inheriting robust switching of charge polarization and a wealth of material choices.

## Ferroelectricity in monolayer graphene/BN heterostructures

While all previous studies focused on spatially distinguishable two-layer graphene, including Bernal[17–20], twisted[4] and BN intercalated bilayer[21] graphene, here we construct a heterostructure consisting of a monolayer graphene encapsulated by WSe₂ (Part A) or BN (Part B) (Fig. 1a). This is because (1) monolayer graphene is a single sheet of two-dimensional electron gas with a well-defined spatial distribution along the out-of-plane direction and (2) WSe₂ has a large lattice mismatch (~30%) with graphene and BN, so any long-period moiré
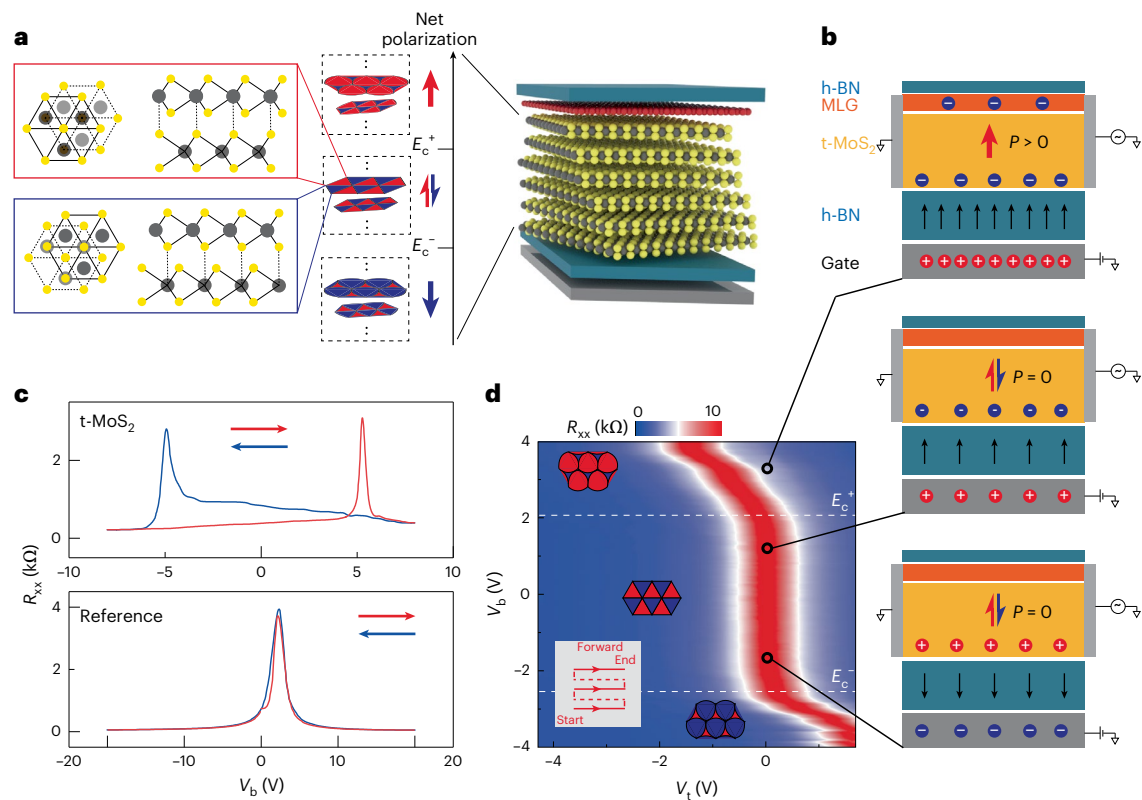
**Fig. 2 | Ferroelectricity observed in multilayer twisted MoS₂. a**, Device schematic of a graphene–MoS₂ heterostructure. Owing to the variation in twisted angles and strain, antiferroelectric domains at each interface will be distinct (two interfaces are schematically plotted). The nearly decoupled interfaces (evidenced in Supplementary Section 10), however, allow for evaluation of the net polarization $P$ by numerically averaging all interfaces. The switching dynamics of domain polarization by electric fields $E_c$ are illustrated. **b**, Working mechanism of Coulomb screening. Three representative states are highlighted by the device schematic, in which t-MoS₂ refers to the multilayer twisted MoS₂ shown in **a**. The gating field (black arrows in the h-BN layer) is screened by the intrinsically electron-doped MoS₂ but can polarize the interfacial ferroelectrics made of MoS₂. The ferroelectric polarization field $P$ subsequently changes the

state of the monolayer graphene on top. Here we show the cases of $E > E_c^+$ (top, $P > 0$), $0 < E < E_c^+$ (middle, $P = 0$) and $E_c^- < E < 0$ (bottom, $P = 0$), where $P = 0$ leaves the graphene undoped. **c**, Top: hysteretic transfer curves are observed when scanning back and forth $V_b$. We emphasize that the hysteresis is not a result from a ferroelectric BN, since another part of graphene without twisted MoS₂ does not show any hysteresis (bottom). **d**, A full phase diagram showing the Coulomb screening regime. The overlaid schematics of polar domain networks are for a single twisted interface; however, owing to the decoupling of adjacent interfaces, the domain wall motion in a multilayer sample can be represented by that of a single interface. Corresponding to schematics in **b**, three representative states are highlighted by black circles. Inset: the gate scanning scheme.

superlattices can be eliminated on the graphene or BN surface. See Supplementary Section 11 for more about the reasoning of comparing ferroelectricity in bilayer and monolayer graphene heterostructures.

Figure 1b,c shows distinct dependences on the top ($V_t$) and bottom ($V_b$) gates, where the hysteretic behaviour is only observed for $V_t$ (see more monolayer devices in Supplementary Figs. 4 and 5 in Supplementary Sections 2 and 3). First, unlike the bilayer graphene, electrons in monolayer graphene cannot be divided into two groups with different physical characteristics or layer distribution, which contradicts previous models such as correlation induced interlayer charge transfer[17] and excitonic ferroelectricity[19,20]. Second, almost identical results are found for Parts A and B. On the one hand, it indicates that WSe₂ plays no role to form ferroelectricity. On the other hand, owing to the absence of moiré superlattices between graphene and WSe₂, it directly proves that a moiré superlattice (at least, the long-periodic one that results in a narrow moiré band) is not necessary, which agrees with previous experiments[18] where the polarized charge density is well beyond the capacity of a moiré band. Actually, in most of the ferroelectric graphene/BN heterostructures[4,17–21], one cannot see the superlattice gap manifested as a satellite resistance peak. In addition, the persistence to room temperature of the hysteresis is unlikely to be a correlation effect (see temperature dependence in Supplementary Figs. 3 and 4). All of these facts lead to a conclusion that the above ferroelectricity

does not stem from the interface between graphene and BN. Instead, it originates from the BN itself.

More specifically, the ferroelectricity originates from the particular BN flake of the hysteretic gate. For clarity, we define the ferroelectric BN as Fe-BN to distinguish it from the normal hexagonal BN (h-BN). To support this argument, we plot a two-dimensional coloured map of resistances versus both gates in Fig. 1d. With abundant Landau levels, the Coulomb screening region (the nearly vertical ridge in parallel with the $V_t$ axis; see strictly vertical ridges in Supplementary Figs. 4 and 5) can be identified for all electronic states as well as charge neutral points (CNP). Obviously, all these features (highlighted by red triangles in Fig. 1d) depend on the magnitude of $V_t$ instead of a displacement field ($D$) involving contributions from both gates. We noticed that ferroelectric devices made of Bernal bilayer[18] or rhombohedral hexalayer (Supplementary Section 6) graphene have a similar dependence, which, again, is in contrast to the electron-driven mechanisms, because the layer polarization of electrons in these multilayer graphene depends on $D$ rather than a single gate.

In Fig. 1d, the ferroelectric gate $V_t$ is taken as the slow scanning axis, where the forward and backward scanning have no hysteresis (Supplementary Fig. 1). Upon changing $V_t$ as a fast scanning gate, a hysteresis loop can be formed by subtracting the backward from the forward scanning (Fig. 1e). The hysteresis magnitude, that is, the range
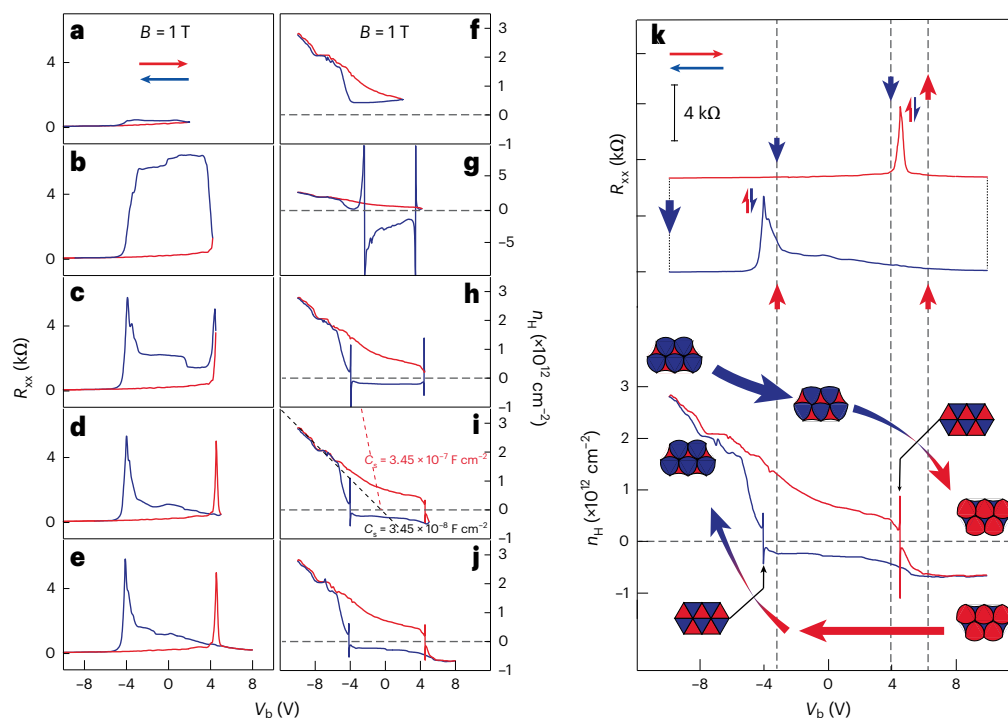
**Fig. 3 | Dynamics of polarization switching. a–j,** Longitudinal resistance (**a–e**) and Hall carrier density (**f–j**) characterization by varying the sweeping range of the positive gate. Here the negative limit of $V_b$ is fixed at −10 V and the positive limit is set as 2 V, 4 V, 4.5 V, 5 V and 8 V, respectively. While positive polarization is not achieved in **a**, the Coulomb screening just happens on the CNP position in **b**. The domain wall dynamics can be best presented in **c**, where the CNP is not accessed during the forward scanning, but the electronic state continues to pass the CNP from hole doping to electron doping in the process of backward scanning (as evidenced in **h**). In **i**, the screened capacitance ($C_s$) of the bottom gate is fitted by a black dashed line, which is distinct from the calculated value for a 10 nm h-BN (red dashed line) as expected. **k,** Illustration of varying charge polarization by arrows (top, $R_{xx}$) and polar domains (bottom, $n_H$) during a full sweeping range.

of Coulomb screening, is found to be significantly larger than that in Fig. 1d. Phenomenologically, the contrast is due to the relatively short relaxation time $\tau$ ~ 4.8 min, that is, the magnitude of charge polarization initiated by a large gate voltage decays with time by itself[18] (see measurements in Supplementary Fig. 1j). As such, the non-hysteretic phase stays in equilibrated states, and the hysteresis loop must take into account dynamics of polarization switching (see Supplementary Figs. 2 and 4h and detailed explanation in Fig. 3). For comparison, a sample with a long relaxation time is shown in Fig. 1f, where a loop remains observable for slowing scanning of the ferroelectric top gate (more data are shown in Supplementary Section 2).

## Reproduced ferroelectric behaviour in multilayer twisted MoS$_2$

So far, the ferroelectric devices investigated have been mainly made of bulk Fe-BN flakes, which are rare among exfoliated flakes from high-quality crystals. By excluding charged defects as the cause of resistance hysteresis (Supplementary Section 8), the only mechanism left for a ferroelectric BN is sliding ferroelectricity between BN layers without AA′ stacking orders. The candidates of Fe-BN structure involve rhombohedral stacking[28] and dislocation-induced moiré superlattices[29–41]. The former is discussed in Supplementary Section 7, and the latter is supported by structural characterizations in Supplementary Section 9. Importantly, the non-AA′ stacking order in BN has been reported to be conductive at grain boundaries with conventional AA′ stacking regions[42]. While at present we have no direct evidences of a conductive network in the Fe-BN, in the following, we should see that a sliding ferroelectric with finite conductance well explains the observation of ferroelectric hysteresis with Coulomb screening.

Here MoS$_2$ is used to construct sliding ferroelectrics by stacking multiple times with small twist angles (Fig. 2a; see another device in

Supplementary Fig. 10 of Supplementary Section 5). We stress that the twisted multilayer MoS$_2$ is not aiming at simulating the Fe-BN on a structural level, because it is difficult to precisely control twisted angles and strain to be uniform at each interface of the former and it remains challenging to determine the atomic structure of the latter. Rather, a sliding ferroelectric with substantial polarization is sufficient to give more insight of the working mechanism. At each moiré interface, there is a network of triangular domains separated by topologically protected domain walls. Each domain is positively or negatively polarized along the out-of-plane direction owing to the non-centrosymmetric configuration, which are illustrated in top and cross-sectional views. They are arranged in an antiferroelectric way, so that without external electric field the averaged polarization of these two polar domains is nulled. When the $E$ field exceeds a threshold value[25,26], for example, $E_c^+$, the positively polarized domain starts to grow in area via domain wall motion, and the negatively polarized domain shrinks correspondingly.

Now we extend the above picture to multilayer MoS$_2$. Unlike the bilayer case, the uncontrolled variation of twisted angles and inevitable strain between many interfaces makes it difficult to obtain exactly the same domain pattern within the whole heterostructure. Note that the antiferroelectric arrangement in Fig. 2a should not be taken to be exact after averaging all interfaces. Nevertheless, owing to the nearly decoupling between neighbouring interfaces (Supplementary Section 10), the polar domains of a single interface (arranged in the antiferroelectric pattern) can be used to schematically illustrate the dynamics of multiple interfaces. By omitting the details, we define the cumulative polarization as a single parameter $P$ (Fig. 2b). As MoS$_2$ is naturally electron doped by sulfur vacancies, the multilayer stack can be viewed as an additional conductive channel in parallel with graphene. On the one hand, when it is grounded by the graphene, the bottom gating field is expected to be screened: owing to the relatively large density of
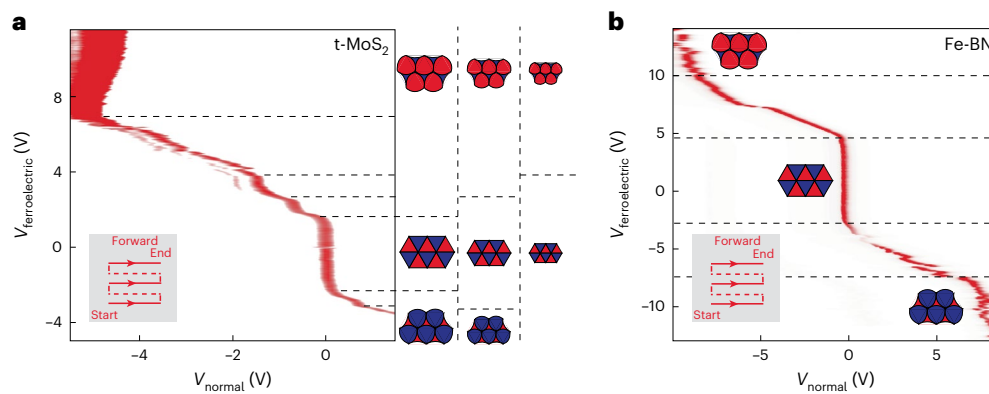
**Fig. 4 | Ladders of ferroelectricity. a**, Multiple ladders of Coulomb screening observed in the phase diagram of the multilayer twisted MoS$_2$ device. Schematic is attached for layer-resolved switching of polar domain networks, where smaller domains require higher switching fields. **b**, Phase diagram for a typical

BN–graphene heterostructure, in which fewer ladders indicate more homogeneous distribution of polar domains. Insets: the gate scanning configuration. Note that, here a unified labelling of $V_{ferroelectric}$ and $V_{normal}$ is used in different types of devices, standing for the gates with and without a hysteresis loop, respectively.

states on the Fermi surface of multilayer MoS$_2$ conductor, the chemical potential is expected to be unchanged by the bottom gate. Thus, the electric field between the MoS$_2$ and the graphene detector is basically determined by the polarization field of ferroelectric MoS$_2$ (see more schematics in Supplementary Fig. 8, Supplementary Section 4). On the other hand, the contribution of MoS$_2$ to the measured conductance can be omitted, owing to the much larger mobility and higher work function of graphene. In other words, the bottom gate switches ferroelectric polarization of twisted MoS$_2$, which sequentially controls graphene conductance.

To verify the proposed scenario, we constructed a heterostructure with hexalayer twisted MoS$_2$. As shown in Fig. 2c, a significant hysteresis could be observed. The reference sample (monolayer graphene on the same BN flake but without MoS$_2$; Supplementary Fig. 6) does not show any hysteresis. The comparison indicates that the ferroelectricity indeed stems from the twisted MoS$_2$. The salient feature—Coulomb screening—is presented in Fig. 2d. In the phase diagram, schematic polar domain networks are overlaid to explain the main features. Corresponding to the schematics in Fig. 2b and Supplementary Fig. 8, the results can be explained as follows. (1) Within the range $[E_c^-, E_c^+]$ of $V_b$, the polar domains are equal along positive and negative directions, leading to a zero polarization field. As the gating field of $V_b$ is screened by the grounded MoS$_2$, the graphene detector is fully controlled by $V_t$ and always stays at CNP when $V_t = 0$ (middle and bottom panels in Fig. 2b). (2) When the gating field of $V_b$ goes beyond the threshold, domain walls will be driven to expand one of the polar domains, which results in nonzero averaged polarization. Although the bottom gating field remains to be screened, the finite polarization field of ferroelectric MoS$_2$ starts to dope the graphene (top panel in Fig. 2b and also Supplementary Fig. 8), which can be evidenced by the shift of CNP along the $V_t$ axis. Consequently, in this regime, the trace of CNP (or the slope of the high-resistance ridge) is determined by the gate dependence of polarization field. This is conceptually different from a non-ferroelectric device, where the trace of CNP reflects the capacitance ratio between top and bottom gates.

## Charge polarization dynamics

An important observation of the Coulomb screening in Fig. 2d is that the forward and backward scanning of $V_b$ do not exhibit a hysteresis loop (similar to that in Supplementary Fig. 1a–c), which apparently contradicts with the strong hysteresis in Fig. 2c. The distinct behaviours are due to the extremely slow scanning rate in the former (~0.14 mV s$^{-1}$) and much faster scanning in the latter (~50 mV s$^{-1}$). To fully understand the relation, we now examine the dynamics of charge polarization.

The longitudinal resistance ($R_{xx}$) and Hall density ($n_H$) are recorded at $B = 1$ T in Fig. 3a–e and Fig. 3f–j, respectively. In each loop, we first

set a fixed negative charge polarization ($V_b$ swept to −10 V) and then scan $V_b$ to different positive values ($V_b^{max}$). Representative results are shown as follows (more data in Supplementary Fig. 9). (1) For a small $V_b^{max} = 2$ V, the charge polarization is always strongly negative within the full loop, leading to small resistances (Fig. 3a) and substantial hole carriers (Fig. 3f). This can be understood, since the positive field is not sufficiently large to trigger the domain wall motion for flipping the negative polarization. (2) With a larger $V_b^{max} = 4.5$ V (Fig. 3c), CNP cannot be accessed during the forward scanning (red curve), as also seen from the positive $n_H$ in the forward scanning (Fig. 3h). When $V_b$ is swept backwards (blue curve), the resistance continues to increase and quickly passes the CNP peak; correspondingly, the carrier type changes from hole to electron. A straightforward scenario is that the domain wall starts to move under the large electric field and it does not stop even when $V_b$ turns back after reaching $V_b^{max}$. Interestingly, it is during the backward scanning that the domain wall passes the neutral position (denoted by the CNP peak and $n_H = 0$). (3) Further increasing $V_b^{max} > 5$ V, CNP can be easily reached in the forward scanning, as evidenced by the peak resistance (Fig. 3d,e) and zero Hall density (Fig. 3i,j).

We emphasize again that the Coulomb screening corresponds to the constant polarization magnitude (that is, domain wall is pinned) and the seemingly 'gate working region' corresponds to the varying polarization via domain wall motion. So in Fig. 3k, we can label the schematic domain patterns for a typical full hysteresis loop. Several features should be stressed. (1) Taking the backward scanning as an example, the pinning of domain wall takes place whenever the scanning is reversed from forward to backward direction, which reflects the retention of the polarized domain. (2) Once the depinning process is initiated, the domain wall motion directly reverses the polarization without a wide zero-polarization region (that is, $[E_c^-, E_c^+]$ in Fig. 2d), resulting a sharp CNP peak. This may be attributed to the inertia of domain wall. (3) For $V_b < -6$ V, the domain wall is not pinned but moves with the magnitude of $V_b$, as seen from the varying $n_H$. However, it is nearly pinned in the window of [−4 V, 4 V]. Understanding of these details about pinning–depinning needs more investigation of domain wall dynamics[16,24–27].

## Ladders in the phase diagram

An interesting feature of multilayer interfacial ferroelectricity is the quantized ladders of charge polarization, thanks to the strongly confined dipoles at each interface[15]. The critical electric field that switches the polar domains may vary at different interfaces. This is reasonable, since the twisted angle determines the dynamics of domain wall but it is difficult to keep the same angle in multilayer moiré superlattices. Consequently, in our multilayer twisted MoS$_2$, a multilevel ladder is

expected. To observe the full phase diagram, the gate scanning range is greatly expanded (Fig. 4a). Several features of Coulomb screening can be found, indicating the pinning of domain walls in these regions. We thus propose a model of interface-specific switching of polar domains, which is schematically shown at every transition point. After polarizing all the interfaces, the graphene ends up with Coulomb screening.

Nevertheless, the ladder can be suppressed in a uniformly stacked three-dimensional moiré superlattice. Here we plot a characteristic phase diagram for ferroelectric BN heterostructures in Fig. 4b. Although the state is a little unstable under a very large electric field (top left and bottom right corners), one can identify that the graphene eventually enters into the region of Coulomb screening. The lack of intermediate ladders suggests that the twisted angles are uniform across all relevant interfaces. Recently, three-dimensional moiré superlattices have been directly synthesized taking advantages of screw dislocation[29–41]. With the finely controlled twisted angle, such a spiral structure is promising to serve as a universal ferroelectric substrate with Coulomb screening.

## Conclusion

In this Article, we establish that the observed ferroelectricity with Coulomb screening in different vdW heterostructures made from monolayer graphene, BN dielectric layers and transition metal dichalcogenides originates from sliding ferroelectrics with finite conductance. These findings remove the stringent limitations to device construction, for example, precise twist angles, or limited choice of constituent materials. First, the monolayer graphene of ferroelectric heterostructures acts as a detector. It is unnecessary to be crystallographically aligned with the encapsulation materials, and can be replaced by any materials that are sensitive to electric gating. For instance, when a Bernal bilayer or twisted bilayer graphene is used, the ferroelectric switching of their intrinsic properties, including CNP peaks, topological phases and superconductivity[4,17–21], should be reproduced. Second, the constituent layer of interfacial ferroelectricity can be expanded to a large family of non-polar vdW materials, including the BN and transition metal dichalcogenides ($MX_2$ with M = Mo, W; X = S, Se, Te), as long as they are doped to be conductive. With recent advances in wafer-scale monolayer synthesis[43–45] and stacking techniques[31,46–48], ferroelectric devices with Coulomb screening may enable large-scale arrays for memory-based networks, promoting the realization of real-word applications with biomimicking functionalities or in-memory computing.

## Online content

Any methods, additional references, Nature Portfolio reporting summaries, source data, extended data, supplementary information, acknowledgements, peer review information; details of author contributions and competing interests; and statements of data and code availability are available at https://doi.org/10.1038/s41565-024-01846-4.

## References

1.  Li, L. & Wu, M. Binary compound bilayer and multilayer with vertical polarizations: two-dimensional ferroelectrics, multiferroics, and nanogenerators. *ACS Nano* **11**, 6382–6388 (2017).
2.  Zhang, D., Schoenherr, P., Sharma, P. & Seidel, J. Ferroelectric order in van der Waals layered materials. *Nat. Rev. Mater.* **8**, 25–40 (2023).
3.  Wang, C., You, L., Cobden, D. & Wang, J. Towards two-dimensional van der Waals ferroelectrics. *Nat. Mater.* **22**, 542–552 (2023).
4.  Klein, D. R. et al. Electrical switching of a bistable moiré superconductor. *Nat. Nanotechnol.* **18**, 331–335 (2023).
5.  Jindal, A. et al. Coupled ferroelectricity and superconductivity in bilayer Td-MoTe₂. *Nature* **613**, 48–52 (2023).
6.  Kang, K. et al. Switchable moiré potentials in ferroelectric WTe₂/WSe₂ superlattices. *Nat. Nanotechnol.* **18**, 861–866 (2023).
7.  Wu, Q., Kang, L., Wu, J. & Lin, Z. Large sliding regulation in van der Waals layered nonlinear optical ternary chalcogenides. *npj Comput. Mater.* **9**, 1–10 (2023).
8.  Fei, Z. et al. Ferroelectric switching of a two-dimensional metal. *Nature* **560**, 336–339 (2018).
9.  Vizner Stern, M. et al. Interfacial ferroelectricity by van der Waals sliding. *Science* **372**, 1462–1466 (2021).
10. Yasuda, K., Wang, X., Watanabe, K., Taniguchi, T. & Jarillo-Herrero, P. Stacking-engineered ferroelectricity in bilayer boron nitride. *Science* **372**, 1458–1462 (2021).
11. Woods, C. R. et al. Charge-polarized interfacial superlattices in marginally twisted hexagonal boron nitride. *Nat. Commun.* **12**, 347 (2021).
12. Rogée, L. et al. Ferroelectricity in untwisted heterobilayers of transition metal dichalcogenides. *Science* **376**, 973–978 (2022).
13. Weston, A. et al. Interfacial ferroelectricity in marginally twisted 2D semiconductors. *Nat. Nanotechnol.* **17**, 390–395 (2022).
14. Wang, X. et al. Interfacial ferroelectricity in rhombohedral-stacked bilayer transition metal dichalcogenides. *Nat. Nanotechnol.* **17**, 367–371 (2022).
15. Deb, S. et al. Cumulative polarization in conductive interfacial ferroelectrics. *Nature* **612**, 465–469 (2022).
16. Ko, K. et al. Operando electron microscopy investigation of polar domain dynamics in twisted van der Waals homobilayers. *Nat. Mater.* **22**, 992–998 (2023).
17. Zheng, Z. et al. Unconventional ferroelectricity in moiré heterostructures. *Nature* **588**, 71–76 (2020).
18. Niu, R. et al. Giant ferroelectric polarization in a bilayer graphene heterostructure. *Nat. Commun.* **13**, 6241 (2022).
19. Zheng, Z. et al. Electronic ratchet effect in a moiré system: signatures of excitonic ferroelectricity. Preprint at https://doi.org/10.48550/arXiv.2306.03922 (2023).
20. Yan, X. et al. Moiré synaptic transistor with room-temperature neuromorphic functionality. *Nature* **624**, 551–556 (2023).
21. Wang, Y. et al. Ferroelectricity in hBN intercalated double-layer graphene. *Front. Phys.* **17**, 43504 (2022).
22. Sharma, P. et al. A room-temperature ferroelectric semimetal. *Sci. Adv.* **5**, eaax5080 (2019).
23. de la Barrera, S. C. et al. Direct measurement of ferroelectric polarization in a tunable semimetal. *Nat. Commun.* **12**, 5298 (2021).
24. Van Winkle, M. et al. Engineering interfacial polarization switching in van der Waals multilayers. *Nat. Nanotechnol.* **19**, 751–757 (2024).
25. Lv, M. et al. Spatially resolved polarization manipulation of ferroelectricity in twisted hBN. *Adv. Mater.* **34**, 2203990 (2022).
26. Lv, M. et al. Multiresistance states in ferro- and antiferroelectric trilayer boron nitride. *Nat. Commun.* **15**, 295 (2024).
27. Molino, L. et al. Ferroelectric switching at symmetry-broken interfaces by local control of dislocations networks. *Adv. Mater.* **35**, 2207816 (2023).
28. Yang, T. H. et al. Ferroelectric transistors based on shear-transformation-mediated rhombohedral-stacked molybdenum disulfide. *Nat. Electron.* **7**, 29–38 (2024).
29. Wang, Z.-J. et al. Conversion of chirality to twisting via sequential one-dimensional and two-dimensional growth of graphene spirals. *Nat. Mater.* **23**, 331–338 (2024).
30. Zhao, Y. et al. Supertwisted spirals of layered materials enabled by growth on non-Euclidean surfaces. *Science* **370**, 442–445 (2020).
31. Castellanos-Gomez, A. et al. Van der Waals heterostructures. *Nat. Rev. Methods Prim.* **2**, 1–19 (2022).
32. Martin, J. W. et al. Graphite rapidly forms via annihilation of screw dislocations. *Carbon* **215**, 118386 (2023).
33. Ci, P. et al. Breaking rotational symmetry in supertwisted WS₂ spirals via moiré magnification of intrinsic heterostrain. *Nano Lett.* **22**, 9027–9035 (2022).

34. Park, H. J. et al. Double-spiral hexagonal boron nitride and shear strained coalescence boundary. *Nano Lett.* **19**, 4229–4236 (2019).

35. Liu, Y. et al. Helical van der Waals crystals with discretized Eshelby twist. *Nature* **570**, 358–362 (2019).

36. Tay, R. Y. et al. Concentric and spiral few-layer graphene: growth driven by interfacial nucleation vs screw dislocation. *Chem. Mater.* **30**, 6858–6866 (2018).

37. Shearer, M. J. et al. Complex and noncentrosymmetric stacking of layered metal dichalcogenide materials created by screw dislocations. *J. Am. Chem. Soc.* **139**, 3496–3504 (2017).

38. Ly, T. H. et al. Vertically conductive $MoS_2$ spiral pyramid. *Adv. Mater.* **28**, 7723–7728 (2016).

39. Sarma, P. V., Patil, P. D., Barman, P. K., Kini, R. N. & Shaijumon, M. M. Controllable growth of few-layer spiral $WS_2$. *RSC Adv.* **6**, 376–382 (2015).

40. Zhang, L. et al. Three-dimensional spirals of atomic layered $MoS_2$. *Nano Lett.* **14**, 6418–6423 (2014).

41. Chen, L. et al. Screw-dislocation-driven growth of two-dimensional few-layer and pyramid-like $WSe_2$ by sulfur-assisted chemical vapor deposition. *ACS Nano* **8**, 11543–11551 (2014).

42. Park, H. J. et al. One-dimensional hexagonal boron nitride conducting channel. *Sci. Adv.* **6**, eaay4958 (2020).

43. Zhao, T. et al. Substrate engineering for wafer-scale two-dimensional material growth: strategies, mechanisms, and perspectives. *Chem. Soc. Rev.* **52**, 1650–1671 (2023).

44. Xu, X. et al. Growth of 2D materials at the wafer scale. *Adv. Mater.* **34**, 2108258 (2022).

45. Zhang, L., Dong, J. & Ding, F. Strategies, status, and challenges in wafer scale single crystalline two-dimensional materials synthesis. *Chem. Rev.* **121**, 6321–6372 (2021).

46. Wang, W. et al. Clean assembly of van der Waals heterostructures using silicon nitride membranes. *Nat. Electron.* **6**, 981–990 (2023).

47. Li, H. et al. Constructing van der Waals heterostructures by dry-transfer assembly for novel optoelectronic device. *Nanotechnology* **33**, 465601 (2022).

48. Frisenda, R. et al. Recent progress in the assembly of nanodevices and van der Waals heterostructures by deterministic placement of 2D materials. *Chem. Soc. Rev.* **47**, 53–68 (2018).

¹State Key Laboratory for Mesoscopic Physics, School of Physics, Peking University, Beijing, China. ²Institute of Microelectronics, Chinese Academy of Sciences, Beijing, China. ³School of Physical Sciences and CAS Key Laboratory of Vacuum Physics, University of Chinese Academy of Sciences, Beijing, China. ⁴National Engineering Research Center of Electromagnetic Radiation Control Materials, School of Electronic Science and Engineering, University of Electronic Science and Technology of China, Chengdu, China. ⁵Laboratory of Advanced Materials, Department of Materials Science, Collaborative Innovation Center of Chemistry for Energy Materials (iChEM), Fudan University, Shanghai, China. ⁶School of Physical Science and Technology, ShanghaiTech University, Shanghai, China. ⁷State Key Laboratory of Quantum Optics and Quantum Optics Devices, Institute of Opto-Electronics, Shanxi University, Taiyuan, China. ⁸National Institute for Materials Science, Tsukuba, Japan. ⁹School of Physical Sciences and CAS Center for Excellence in Topological Quantum Computation, University of Chinese Academy of Sciences, Beijing, China. ¹⁰State Key Laboratory of Surface Physics and Institute for Nanoelectronic Devices and Quantum Computing, Fudan University, Shanghai, China. ¹¹Zhangjiang Fudan International Innovation Center, Fudan University, Shanghai, China. ¹²School of Physics, Huazhong University of Science and Technology, Wuhan, China. ¹³Liaoning Academy of Materials, Shenyang, China. ¹⁴These authors contributed equally: Ruirui Niu, Zhuoxian Li, Xiangyan Han, Zhuangzhuang Qu. ✉e-mail: hanchunrui@ime.ac.cn; bo_peng@uestc.edu.cn; vitto.han@gmail.com; jmlu@pku.edu.cn

## Methods

### Sample fabrication

Monolayer graphene, few-layer graphite gates, transition metal dichalcogenides and BN (including BN that are later identified to be ferroelectric by electric measurement) flakes were all mechanically exfoliated from bulk crystals onto silicon wafers and identified with optical microscopy. Rhombohedral BN flakes were grown following ref. [49]. Following the recipe in ref. [18], multilayer heterostructures were then fabricated according to the standard dry transfer method [50]. Then reactive ion etching was used to pattern the Hall bar geometry. Lastly, one-dimensional edge contacts [51] were prepared following the standard e-beam lithography and e-beam evaporation of Cr (1 nm)/Au (50 nm).

### Electrical measurement

All the transport measurements were carried out in a cryostat equipped with a superconducting magnet up to 9 T. A standard four-probe method of constant current was performed [18]. The a.c. current was supplied by Stanford Research Systems SR830 lock-in amplifiers with a working frequency of 17.777 Hz. The d.c. gate voltages were output by two Keithley 2400 source meters.

## Data availability

The data that support the findings of this study are available within the article and its Supplementary Information. Any other relevant data are available from the corresponding authors upon reasonable request.

## References

49. Qi, J. et al. Stacking-controlled growth of rBN crystalline films with high nonlinear optical conversion efficiency up to 1%. *Adv. Mater.* **36**, 2303122 (2024).
50. Kim, K. et al. Tunable moiré bands and strong correlations in small-twist-angle bilayer graphene. *Proc. Natl Acad. Sci. USA* **114**, 3364–3369 (2017).
51. Wang, L. et al. One-dimensional electrical contact to a two-dimensional material. *Science* **342**, 614–617 (2013).

## Acknowledgements

## Author contributions

## Competing interests

The authors declare no competing interests.

## Additional information

**Supplementary information** The online version contains supplementary material available at https://doi.org/10.1038/s41565-024-01846-4.

**Correspondence and requests for materials** should be addressed to Chunrui Han, Bo Peng, Zheng Vitto Han or Jianming Lu.

**Peer review information** *Nature Nanotechnology* thanks the anonymous reviewers for their contribution to the peer review of this work.

**Reprints and permissions information** is available at www.nature.com/reprints.